1

2   **REVISION 1**

3   **Reflectance spectroscopy and optical functions for hydrated Fe-sulfates**

4   Karly M. Pitman[1,*], Eldar Z. Noe Dobrea[1], Corey S. Jamieson[2], James B. Dalton III[3],

5   William J. Abbey[3], and Emily C. S. Joseph[1]

6   [1]Planetary Science Institute, 1700 E. Fort Lowell Road., Suite 106, Tucson, Arizona

7   85719, U. S. A.

8   [2]SETI Institute, 189 Bernardo Ave., Ste. 100, Mountain View, California 94043, U. S. A.

9   [3]Jet Propulsion Laboratory, California Institute of Technology, 4800 Oak Grove Drive,

10   Pasadena, California 91109, U. S. A.

11   [*]E-mail: pitman@psi.edu

12   **Abstract**

13   Visible and near-infrared wavelength (VNIR, λ=0.35 - 5 µm) laboratory diffuse

14   reflectance spectra and corresponding optical functions (real and imaginary refractive

15   indices) for several iron sulfates (natural K- and Na-jarosite, szomolnokite, rhomboclase)

16   are presented. On Mars, jarosite has been identified in Meridiani Planum, Mawrth Vallis,

17   Melas Chasma, and Eridania Basin; szomolnokite has been found as distinct layers at

18   Columbus Crater and as outcrops at Juventae Chasma, and rhomboclase has been

19   identified at Gusev Crater. Constraining the mineralogy and chemistry (Fe- vs. Mg-rich)

20   of the sulfates on Mars may contribute to our understanding of the environmental and

21   aqueous conditions present on Mars during their formation. The data presented here will

22   help to constrain the mineralogy, abundance, and distribution of sulfates on the martian

23   surface, which will lead to improvements in understanding the pressure, temperature, and

24   humidity conditions and how active frost, groundwater, and atmospheric processes once

25   were on Mars.

26   **Keyword:** jarosite, szomolnokite, rhomboclase, optical constants, visible to near-infrared

27   wavelength, laboratory diffuse reflectance spectroscopy

28

29   Introduction

30   Iron sulfates, hereafter Fe-sulfates, have been observed spectroscopically on Mars

31   in a variety of forms via Earth-based telescope observations as well as spacecraft, landed,

32   and rover missions. This suggests that acidic aqueous conditions occurred in the past and

33   that evaporation and dessication processes were at work on Mars.

34   Sulfate minerals have been inferred for Mars since the Viking and Pathfinder

35   spacecraft missions (e.g., Toulmin et al. 1977; Kieffer et al. 1992 and references therein)

36   and have been found in the Mars-derived SNC meteorite class (e.g., Chatzitheodoridis

37   and Turner 1990; Gooding 1992; Treiman 1993; Bridges and Grady 2000; Bridges et al.

38   2001; Wentworth et al. 2002, 2005; Farquhar et al. 2007). A variety of sulfates have also

39   been directly observed on Mars at near- and thermal-IR wavelengths using the NASA

40   Infrared Telescope Facility in Hawaii and from Mars orbiter and landed mission

41   instrumentation including the Phobos 2 infrared imaging spectrometer (ISM), Mars

42   Global Surveyor Thermal Emission Spectrometer (MGS TES), Mars Exploration Rovers

43   (MER) Spirit and Opportunity, Mars Express Observatoire pour la Mineralogie, l'Eau, les

44   Glaces et l'Activite (OMEGA), and Mars Reconnaissance Orbiter Compact

45   Reconnaissance Imaging Spectrometer for Mars (MRO CRISM) (Pollack et al. 1990;

46   Blaney and McCord 1995; Bandfield 2002; Cooper and Mustard 2002; Bibring et al.

3

47   2004; Lane et al. 2004, 2008; Squyres et al. 2004; Johnson et al. 2007; Murchie et al.

48   2007). Observations performed with the Mars Exploration Rovers (MER) and Mars

49   Express OMEGA visible and near-infrared imaging spectrometer led to the discovery of

50   hydrated sulfates exposed in outcrops on the martian surface (e.g., Squyres et al. 2004;

51   Gendrin et al. 2005; Bibring et al. 2006). Observations performed at a higher spatial

52   resolution with MRO CRISM led to the discovery of many more small (kilometer-sized)

53   hydrate-bearing outcrops scattered throughout the martian surface (e.g., Pelkey et al.

54   2007; Murchie et al. 2009). The diversity of hydrated phases on Mars overall suggests an

55   aqueous history where water was present in a large variety of geological environments

56   and pH levels.

57   Several Fe-bearing sulfate minerals are of particular interest for Mars research.

58   Fe-sulfates have been found only in specific areas (e.g., Lichtenberg et al. 2010; Roach et

59   al. 2010; Ling and Wang 2010 and references therein; Liu and Wang 2012 and references

60   therein). Pathways to the formation of Fe-hydroxides and other Fe-sulfates such as

61   melanterite and jarosite by weathering sulfides, acid fog alteration, and Fe-oxidation have

62   been suggested for Mars (e.g., King and McSween 2005; Golden et al. 2005; Tosca et al.

63   2008 and references therein). Fe-sulfates were found by the MER rovers in a variety of

64   forms, including jarosite, in Meridiani Planum and Gusev Crater, suggesting that acidic

65   aqueous, evaporation, and dessication processes were at work in these locations (Fairen et

66   al. 2009 and references therein). Jarosite outcrops have also been found in Mawrth Vallis

67   (Farrand et al. 2009) and western Melas Chasma (Weitz et al. 2009, 2012, 2013).

68   Szomolnokite and jarosite have been found as distinct layers within polyhydrated non-Fe

69   sulfate at Columbus Crater on Mars (Wray et al. 2008, 2009a), and hydrated Fe-sulfates

4

70   have been positively identified in the martian southern highlands and Endeavour Crater in

71   Meridiani Planum (Wray et al. 2009b,c). Szomolnokite has been suggested as a possible

72   match for the monohydrated sulfate at Aram Chaos (Lichtenberg et al. 2010). Juventae

73   Chasma, located northeast of Valles Marineris, also matches spectral signatures of mono-

74   and polyhydrated sulfates, including szomolnokite, dehydrated ferric sulfate and

75   copiapite, and hydronium jarosite (Bishop et al. 2008, 2009; Bishop and Weitz 2011).

76   Jarosite, rozenite, and szomolnokite have been definitively identified on Mars by

77   OMEGA and CRISM (Carter et al. 2013). X-ray diffraction results from temperature

78   series experiments of dehydrating ferrous sulfates (melanterite, rozenite, szomolnokite,

79   halotrichite, and romerite) suggest that melanterite might be unstable under Martian

80   surface conditions, but other ferrous sulfates, including szomolnokite, should be stable

81   (Brown et al. 2008). Rhomboclase has been extensively investigated in stability field

82   studies of Mars minerals (e.g., Wang and Ling 2011 and references therein).

83   Rhomboclase and other Fe-sulfates (hydronium jarosite, ferricopiapite, paracoquimbite,

84   fibroferrite) have been suggested for Mars based on MER Pancam and laboratory spectral

85   analyses (Johnson et al. 2007; Lane et al. 2008; Ling and Wang 2010 and references

86   therein). Whereas the sulfate chemical varieties (Fe-, Mg-, Ca-bearing) on Mars may be

87   caused by acidic surface water, some of these (Mg-sulfates) do not require acidic surface

88   water to form, so determining the exact type of Mars sulfates (Fe- vs. Mg-rich) may lead

89   to critical information on the epoch of their formation or humidity conditions on Mars

90   during their formation (Marion and Farren 1999; King and McSween 2005; Vaniman et

91   al. 2004; Cloutis et al. 2007).

92   Although the presence of sulfates and hydrous alteration minerals on Mars

93   strongly suggests that Mars experienced at least one period of aqueous activity at some

94   point in its history, the extent of this activity is still not fully understood: Was alteration

95   extensive to the point that aqueous minerals became the dominant mineralogical species

96   in the areas where alteration occurred, or was it limited such that the alteration products

97   now form a small part of a mineral assemblage that includes unaltered primary minerals?

98   In order to resolve this issue, it is necessary to constrain the type and abundance of

99   aqueous and non-aqueous minerals present in an assemblage. Laboratory diffuse

100   reflectance spectra may be used to constrain surface abundance to first order via linear

101   mixture modeling of spacecraft observations, in which the spacecraft spectrum is

102   modeled as a linear combination of laboratory spectra of individual minerals, scaled by

103   their abundances (cf. Ramsey and Christensen 1998). This method is primarily

104   applicable in the mid-infrared ($\lambda \sim$ 5-50 μm), where minerals present a very low albedo

105   (0.12-0.14 for unaltered minerals) and light that undergoes multiple reflections is

106   commonly absorbed before it can escape the assemblage. When minerals are intimately

107   mixed, such that light reflects off of multiple surfaces before escaping to the observer, or

108   when materials have a higher albedo, which occurs in the visible and near-infrared (λ

109   ~0.35-5 μm) portion of the electromagnetic spectrum, spectral mixing is non-linear.

110   Radiative transfer theory (e.g., Hapke 1993, 2002, 2008; Shkuratov et al. 1999) can be

111   used to model the spectra of such intimate mixtures. These models rely on the optical

112   functions, or "constants" (real and imaginary refractive indices $n(\lambda)$ and $k(\lambda)$) of the

113   materials involved, which can be derived from laboratory spectra of grain size separates.

114   Availability of reflectance spectra and optical constants for Fe-sulfates will enable

115   detailed analysis of remote and landed spectral observations, improving our

116   understanding of the physical and chemical evolution of the Martian surface. Therefore,

117   in this study, we present both laboratory visible to near-infrared (λ ~0.35-5 μm) diffuse

118   reflectance spectra and derived optical constants of a suite of Mars-relevant Fe-sulfates.

119   Prior Work

120   Whereas the full range of Fe-sulfate chemistries has been explored in detail with

121   Raman, LIBS, Mossbauer, reflectance, absorption, and emissivity spectroscopy, few

122   optical constant datasets exist for hydrated Fe-sulfates, largely because few reflectance

123   spectral datasets have been published with robust particle size estimates. Diffuse

124   reflectance spectra, especially in the visible to near-infrared wavelength (VNIR) range,

125   exist for Fe-sulfates (Table 1), typically at standard temperature and pressure conditions

126   for Earth. For this work, we surveyed the literature and also several spectral databases in

127   use by Mars researchers to determine which Fe-sulfates and grain sizes would be the

128   most useful to add to known holdings. The PDS Geosciences Node Spectral Library

129   (http://speclib.rsl.wustl.edu/) yielded Fe-sulfate samples in < 45 μm and < 125 μm size

130   fractions. The ASTER spectral library (Advanced Spaceborne Thermal Emission and

131   Reflection Radiometer, http://speclib.jpl.nasa.gov) contains only < 45 μm, 45-125 μm,

132   125-500 μm samples of jarosite, plumbojarosite, and natrojarosite. The HOSERLab

133   collection (Hyperspectral Optical Sensing for Extraterrestrial Reconnaissance Laboratory,

134   http://psf.uwinnipeg.ca/Sample_Database.html; E. Cloutis, pers. comm. 2013) offers a

135   wide variety of Fe-sulfate compositions, but these are only available for one size fraction:

136   < 45 μm. Brown University's RELAB database (Reflectance Experimental Laboratory,

137   http://www.planetary.brown.edu/relabdata/catalogues/Spectra_Catalogue.xls) repeats

138   many of the HOSERLab samples, as well as additions from contributors such as J.

139   Bishop, M. Lane, J. Mustard, and R.V. Morris. A few studies have varied pressure-

140   temperature or dehydration conditions to resemble Mars but at the expense of measuring

141   multiple particle sizes. Overall, few past studies acquired reflectance spectra for multiple

142   grain sizes or even documented the grain size of the samples; those that did document

143   sizes listed the sieve fractions used to produce their samples, which were often either

144   extremely broad or open-ended (e.g., < 45 µm), suggesting that the mean effective

145   diameter is unknown, with sizes likely dominated by clumps and the finest particles in

146   the sample. This is problematic for four reasons: (1) At least three grain sizes are

147   essential for deriving optical functions that can be used to generate models of different

148   grain sizes (e.g., Lucey 1998). (2) Sieve fractions are rough-cut estimates of grain size;

149   for sieved particulates, the mean effective diameter of a sample can be much different

150   than the median value of the sieve fraction limits (~20% larger than the upper screen size;

151   Moersch & Christensen 1995). (3) Knowing the grain size well is important because it is

152   the main variable and largest source of error in determining optical constants. (4) The

153   particle sizes in past studies fall into two categories, motivated by IRTM/TES and MER

154   results: atmospheric dust/silt-sized (e.g., < 45 µm size fraction) or sand-sized (~ 200 µm).

155   However, for aqueous terrains such as fluvial and lacustrine deposits, there should be a

156   range of particle sizes between and greater than those diameters, up to mm-scale or

157   gravel sizes (Folk 1974). Thus, there is a need for laboratory reflectance spectra that

158   represent Mars equatorial surface temperatures (T ~ 280-300 K) and different particle

159   sizes that have not been measured before, to better represent aqueous terrains and

160   converge on the best set of optical constants (which should be independent of particle

161   size). Thus, we concentrated on four hydrated Fe-sulfate minerals for which sieve

162   fractions were typically broad in past literature (Table 2) and six finite size fractions

163   between 53 and 250 µm (Table 3) to fill in the missing size range between atmospheric

164   dust and sand-sized particles.

165   Experimental Details

166   Table 2 lists the samples measured in this study. A larger suite of Fe-sulfates of

167   different hydration types was purchased from Excalibur Minerals and Minerals

168   Unlimited, including some of the same lots previously measured for the Mars program.

169   Upon X-ray diffraction (XRD) analysis, it was determined that many of these samples

170   were contaminated with mixed phases or rinds. We present data on the purest samples

171   from the original Excalibur / Minerals Unlimited suite (natural K-jarosites from three

172   localities and rhomboclase), a natural powdered sample of Na-jarosite (Caltech

173   collection, courtesy of Drs. Joel Hurowitz and Ken Farley), and synthesized samples

174   (szomolnokite). The szomolnokite was synthesized by putting ferrous sulfate in an oven

175   at 80°C until it reached chemical stability.

176   Optical constants may be estimated from spectral measurements of reflectance at

177   multiple particle sizes, or derived from a combination of reflectance and transmittance

178   spectra. In diffuse reflectance spectroscopy, the samples are loosely packed powders

179   having randomly-oriented particles of a known size range. Samples for this study were

180   ground and sieved to consistent particle size ranges. The natural rhomboclase sample

181   (Alcaparrosa, Chile) and Na-jarosite were already in particulate form, so were sieved

182   without crushing; for the remaining samples, all grain sizes > 250 µm were crushed and

183   resieved to the six size fractions in Table 3. The average grain diameters in Table 3 were

184   also verified by optical microscopy in transmitted and reflected light at 10x zoom and

185   analyzed with the particle sizing software suite Simagis Live™, Smart Imaging

186   Technologies, Co., Houston, TX: http://www.simagis.com (Fig. 1), which performs

187   similarly to the ImageJ particle analysis software used for Mars analog clays (e.g., Brown

188   et al. 2012). For our optical microscopy images, the particle detection limit for the

189   Simagis Live^{TM} automated grain size analysis software with intensity threshold set to

190   zero was equivalent spherical particle diameter ~ 1.1-3 μm. Particles with projected

191   areas 0.84 μm^2 (diameter ~ 1.03 μm) and less were rejected as blank pixels. Grain

192   boundaries and overlapping particles were verified both by automated and manual

193   identification of 8-10 fields-of-view per size fraction, yielding the total number of

194   particles per size fraction on the order of 100-1000. The histograms showing the

195   distribution of grain sizes for all samples are available by request. Table 3 summarizes

196   the diameters for the samples, including mode 1 (the dominant grain size by area) and

197   mode 2 (the amount of fines in the sample). Particles with larger geometric cross-

198   sectional area most affect the single scattering phase function; for example, increasing the

199   number of mid-sized particles or adding fines in various proportions to create bimodal or

200   trimodal size distributions in multisphere T-matrix models does not have much effect on

201   the phase function or even the single scattering albedo of collections of loosely or

202   closely-packed Mg-sulfate particles (values change in the 1e-5 place; Pitman et al. 2013).

203   Thus, we assume mode 1 diameters in our n, k derivations.

204

205   Processing of the samples was performed by lightly crushing the materials using a

206   mortar and pestle, and subsequently dry sieving to the size fractions of interest. The

207   synthetic szomolnokite and natural K-jarosite samples were most stable to crushing and

208   sieving. With the exception of the rhomboclase, the Fe-sulfates (notably natrojarosite)

209   formed aggregates and clumps immediately upon sieving. The sieved rhomboclase

210   particles were very transparent and did not readily form aggregates. To avoid changing

211   the hydration state of the sulfates, the samples were not washed; however, under optical

212   microscopy, we saw no evidence of coating with very small fines. Whereas SEM images

213   can provide more detail for particle diameters from 0.01-5 μm (e.g., for monitoring

214   clinging fines in clays; Roush et al. 2013), optical microscopy should suffice for

215   characterizing particle sizes of the order of one to hundreds of microns (Yang, 2003).

216   Due to the fact that the hydration state of some sulfates is very sensitive to

217   environmental humidity and temperature, maintaining the long-term stability of the

218   mineral was an issue of concern. Thus, for the synthesized samples, sample preparation

219   was performed immediately after synthesis under controlled humidity and temperature

220   conditions. Spectral and XRD analyses were performed as quickly as possible after

221   samples were prepared, after they were processed, and after they were measured. For

222   spectral analysis, the prepared hydrated Fe-sulfate powders were placed in stainless steel

223   sample holder cups with sample volume on the order of 2 cm^3 (1 cm depth), to ensure

224   that each material was optically thick in the near-IR.

225   Powder XRD patterns were obtained for all samples using JPL's Bruker AXS model

226   D8 Discover X-ray diffractometer which is equipped with a graphite monochromator and

227   a General Area Detector Diffraction System (GADDS). The radiation applied was CuKα

228   ($\lambda = 1.5404$ Å) operated at 40 kV and 20 mA. The phase identification was confirmed by

229   comparing the 13 to 47° 2θ range (Fig. 2) with standard powder diffraction files from the

230   International Centre for Diffraction Data (ICDD), 2000.

231   Room temperature (T~300 K) diffuse reflectance spectra were acquired at ambient

232   pressure (1 bar) at JPL's Planetary Ices Characterization Laboratory. From $\lambda = 0.35$-2.5

233   μm (resolution: 3 nm for $\lambda < 1$ μm, 10 nm for $\lambda > 1$ μm), diffuse bidirectional reflectance

234   spectra were acquired with an Analytical Spectral Devices Inc.® (ASD) FieldSpec FR[3]

235   fiber optic spectrometer at three viewing geometries (incidence angle i=0°, phase angle g

236   and emergence angle e=10°, 15°; i=30°, g=e=0°) for each of the six grain sizes. A

237   Thermo Scientific® mercury cadmium telluride (MCTA) detector was used to collect

238   conical-hemispherical reflectance spectra at $\lambda = 1.5$-25 μm (resolution: 2 cm^{-1}). Spectral

239   data are truncated at $\lambda \leq 10$ μm due to signal attenuation by CaF_2 infrared windows;

240   however, this exceeds the wavelength range needed for NASA Mars missions. The

241   sample cup was illuminated from above through two separate viewports at 11.5^o relative

242   to normal by two light sources: a globar from a Thermo Scientific® Nicolet 6700 Fourier

243   transform infrared (FT-IR) spectrometer and a Sciencetech Inc.® 650W quartz-tungsten-

244   halogen (QTH) lamp with low-OH silica fiber optics. For each grain size fraction, 25

245   individual spectra were acquired with the ASD FieldSpec 3 and spectrally averaged to

246   produce signal-to-noise ratios of 1000 or better. The spectra were calibrated with two

247   NIST-approved standards: Spectralon® (Labsphere, Inc.) for the VNIR and diffuse

248   InfraGold® for the NIR-MIR range. The NIR-MIR spectra from the MCTA detector

249   were scaled and merged to the VNIR ASD spectra at $\lambda = 2$ μm.

250

251   Spectroscopic Results

252   In Figures 3-5, we present diffuse laboratory reflectance spectra and estimated

253   optical constants for K-jarosite, Na-jarosite, rhomboclase, and szomolnokite. Electronic

254   data tables for all reflectance spectra and optical constants shown are available as a

255   supplement to this article. For K-jarosite (Fig. 3), we first compared the VNIR range for

256   the three different localities, then focused our analyses on the two samples with the

257   greatest range in spectral behavior: Copiapo Mine and Arabia. The Arabia jarosite is the

258   purest in terms of K-jarosite chemistry whereas the Copiapo jarosite dataset is superior in

259   terms of size analysis, as some grain size fractions were excluded from the Arabia

260   jarosite and rhomboclase analyses due to poor sorting or microscopy image quality.

261   Reflectance spectra for Na-jarosite, rhomboclase, and szomolnokite (Fig. 5) are plotted in

262   different wavelength ranges (λ = 0.35 to 2.5, 5, or 10 μm) to illustrate the important

263   peaks for each compound. In Figures 4-5, optical constants are shown in the same VNIR

264   range for best comparison, as the rhomboclase reflectance spectra drop for λ > 2.5 μm.

265   We modeled the laboratory reflectance spectra to derive k using analytic radiative

266   transfer scattering theory, as described in detail in Dalton and Pitman (2012). Briefly, we

267   used the USGS package *radtran* (Clark 1993), which creates synthetic reflectance spectra

268   from the approximation of Hapke (1981, 1993),

269
$$R_{synth} = \frac{\omega}{4\pi} \frac{\mu_0}{\mu + \mu_0} \{[1 + B(g)]P(g) + H(\mu_0)H(\mu) - 1\}. \text{ (Eq. 1)}$$

270   In Eq. 1, ω is the single-scattering albedo, μ_0 and μ are the cosines of the incidence and

271   emergence angles e and e, $H(\mu_0)$ and $H(\mu)$ describe the intensity of the radiation

272   scattered, the backscatter function B(g) depends on phase angle g, opposition surge width

273   and height, and P(g) is the single particle phase function weighted by coefficients b and c.

274   For a given wavelength, we calculated the best ω to make the synthetic spectrum

275   match the laboratory spectrum. Assuming that particles are closely packed, ω is

276
$$\omega = S_E + \frac{(1 - S_E)(1 - S_I)\left\{r + \exp\left[-2(\alpha(\alpha + s))^{1/2}d/3\right]\right\}}{1 - rS_I + (r - S_I)\exp\left\{-2[\alpha(\alpha + s)]^{1/2}d/3\right\}}, \text{(Eq. 2)}$$

277   where S_E and S_I are reflection coefficients defined in terms of n; s is the wavelength-

278   dependent internal scattering efficiency; r is the bihemispherical reflectance; and d is the

279   grain diameter. By supplying the laboratory reflectance spectrum, n_{vis} (from Table 4), s,

280   and d, we obtained $k(\lambda)$ from the absorption coefficient α in units of μm^{-1} (Eq. 3):

281
$$\alpha = \frac{4\pi k}{\lambda}. \text{ (Eq. 3)}$$

282   We assumed the following values in calculating α:

283   (1) Diameter specified in Table 3,

284   (2) Density = 3.09 (K-jarosite), 3.18 (Na-jarosite), 2.23 (rhomboclase), 3.0 g cm^{-3}

285   (szomolnokite). Sources: CRC Handbook of Chemistry and Physics (electronic

286   version, http://www.hbcpnetbase.com, http://www.mindat.org,

287   http://webmineral.com, accessed August 30, 2013),

288   (3) Incidence angle $i = 0°$, emission angle e = phase angle $g = 10°$,

289   (4) $B(g) = 0$ and $P(g) = 1 + b cos(g)$ – see Eq. 1 description,

290   (5) radtran specific settings: $d_f = 0$, $w_0 = 1.8$, $sd = 0.3$. In radtran (Clark 1993), the

291   diameter is a function of a constant scale factor, d_f, and a user-specified

292   wavelength, w_0, that divides the reflectance spectrum into two regimes with lower

293   and higher amounts of photon scattering (see Dalton & Pitman 2012 and

294   references therein). d_f is the grain size that produces the best spectral match for λ

295        $> w_0$ divided by the grain size that produces the best match for $\lambda < w_0$. *sd* is the

296   internal scattering coefficient times particle diameter (i.e., the mean number of

297   scattering events per grain diameter).

298   (6) No preferred orientation of samples for n_{vis} ($\lambda \sim 0.589$ µm), i.e., $n_{vis} = n_{mean} =$

299        $(1/3)(n_\alpha + n_\beta + n_\gamma)$ or $(1/2)(n_\omega + n_\varepsilon)$, where n_α, n_β, n_γ, n_ω, and n_ε are the crystal-

300   axis-specific indices of refraction averaged from standard table values (Table 4).

301   We solved for $n(\lambda)$ at different wavelengths after Warren (1984) using equation 4,

$$n(\lambda_i) = n_{vis} + \frac{2(\lambda_{vis}^2 - \lambda_i^2)}{\pi} P \int_0^\infty \frac{\lambda^2 k(\lambda)}{(\lambda_i^2 - \lambda^2)(\lambda_{vis}^2 - \lambda^2)} d\ln\lambda \text{ (Eq. 4),}$$

303   where "P" denotes the principal part of the integral, and iterate until n and k do not

304   change significantly.

305   Discussion

306   VNIR-MIR band assignments for Fe-sulfates are given in detail by Cloutis et al.

307   (2006), Basciano and Peterson (2008), and Bishop and Murad (2005). Briefly, the Fe-

308   sulfate reflectance spectra in Figures 3 and 5 exhibit a sharp rise from $\lambda = 0.35$ to 5.0 µm,

309   with evidence of an iron band at 0.45 µm, then a broad plateau from 0.5 to 1.0 µm and a

310   broad iron absorption centered near 0.80 µm (Fe^{3+}) to 0.90 µm (Fe^{2+}). Changes in the

311   wavelength position and band shape of certain features ($\lambda \sim 1.4, 1.85, 2.26$ µm) are

312   important diagnostics for identifying K- vs. Na-jarosite and formation temperature

313   (Basciano and Peterson 2007, 2008; Swayze et al. 2008; Spratt et al. 2013 and references

314   therein). Water absorptions may be present at 1.4 and 1.9 µm, though this is not

15

315   necessarily structural water. Figures 3a,b show a water band near λ ~ 1.9 μm that is not

316   characteristic of K-jarosite (but is present for hydronium jarosite), suggesting that the

317   Copiapo jarosite sample is either contaminated with a hydrated material or contains some

318   H_3O^+ substituting for K^+. Our XRD analysis confirmed that the Arabia jarosite is pure K-

319   jarosite (Fig. 2, line a) and that the Copiapo Mine jarosite (Fig. 2, line b) is a blend of K-

320   jarosite and Na- and/or H_3O^+-jarosite with a hydrated mineral contaminant, possibly

321   scorodite. The spectral intensity drops to a minimum near the 3.0 μm water fundamental,

322   suggesting at least some structural water, but the 3.1 μm crystalline ice emission band is

323   rarely present, indicating that the samples were measured above the freezing point of

324   water. S-O overtones and combinations give rise to complex structure in the 4.0-5.0 μm

325   region. Our Arabia and Copiapo jarosite spectra show most or all of the expected

326   features in the λ = 1.2-2.6 μm range: λ ~ 1.46 μm (OH vibration + H_2O absorption);

327   1.514, 1.84, 2.214, 2.26, and 2.296 μm (Fe-OH vibrations); 1.96 μm (H_2O absorption);

328   and 2.38-2.5 μm (($SO_4)_2$ stretching + OH vibration) (cf. Basciano and Peterson 2007,

329   2008). Comparing different source localities in Fig. 3e, all three of the jarosites (Arabia,

330   Copiapo, and Bolivia) exhibit the λ ~ 1.46 and 1.84 μm features, with Copiapo jarosite

331   having the deepest feature. The λ ~ 1.514 μm feature is most on mark for the Bolivia

332   jarosite, whereas the Copiapo jarosite is slightly offset in terms of wavelength position.

333   The λ ~ 1.514 μm feature is weak to nonexistent for the Arabia jarosite. The Bolivia

334   jarosite also presents a λ ~ 1.9 μm hydrated band. The Arabia and Bolivia jarosites have

335   a more pronounced shoulder at λ ~ 2.296 μm and more peaks at λ ~ 2.38-2.5 μm than

336   does the Copiapo jarosite. For jarosite, diagnostic $\nu_3(SO_4)^{2-}$ modes at ~ (1200–1000 cm^-

337   ^{1}) 8.33 – 10 μm and one T_2 mode, the triply degenerate antisymmetric stretch at 1104 cm^-

338   [1] ~ 9.06 μm, also fall within our detectors' wavelength range (Spratt et al. 2013 and

339   references therein). However, the fine particulates within our samples result in feature

340   enhancement (i.e., deeper bands) in the VNIR and features being damped out in the IR,

341   such that features longward of 8 μm in our spectra, including the v_3 and main

342   fundamental modes, cannot be uniquely assigned (M. Lane, personal communication,

343   2013). In general, our jarosite and rhomboclase spectra compare favorably to figure 5 of

344   Swayze et al. (2008) and Liu and Wang (2012), respectively. Our szomolnokite

345   resembles the spectra from Cloutis et al. (2006) as well.

346   Reflectance and single scattering albedo depend on particle size; the final set of

347   optical constants per compound does not. However, by using multiple particle sizes, we

348   have attempted to constrain the envelope of possible absorption coefficient values and

349   better converge on $k(\lambda)$ for the bulk mineral. In Figures 4 and 5, the average optical

350   constants for each Fe-sulfate mineral (solid lines) are bracketed by the estimated error

351   due to the diameter estimates in Table 3. Other sources of uncertainty in $n(\lambda)$ and $k(\lambda)$

352   are the quality of the laboratory reflectance spectra, which we have minimized by using

353   long integration times (~2500 s), and approximations in the radiative transfer derivation.

354   Our natural jarosite $n(\lambda)$ and $k(\lambda)$ are in good agreement with a separate experiment on

355   synthetic jarosites using different codes (Sklute et al. 2013). To our knowledge, there are

356   no other optical constants datasets available for Na-jarosite, rhomboclase, or

357   szomolnokite, making these values unique.

358   The laboratory analog reflectance spectra and optical constants contained here

359   will permit determination of the abundance and distribution of Fe-sulfates, and the

360   mineral assemblages in which they are found. Knowledge of the concentration and

361   locations of these materials will improve understanding of the geochemical evolution of

362   the surface of Mars, contents of past water bodies, from channels to paleolakes; tectonic,

363   atmospheric, and other transport phenomena driving chemical and mineral distributions,

364   and the present state of aqueous and organic chemical processes. The power of models

365   utilizing these measurements will be further amplified in the deployment of future surface

366   and orbital infrared instruments to locate sites of past and/or recent aqueous activity,

367   potential habitats for life, and resources for possible human exploration.

368   Implications

369   The results presented herein will enhance the scientific return of orbiter spacecraft

370   missions by substantially contributing to the spectral databases of analog minerals

371   currently available for Mars. This study is unique because it provides both geometry-

372   controlled reflectance spectra and estimated optical constants for hydrated Fe-sulfates,

373   which can be used as tracers of the past composition and state (e.g., relative humidity,

374   oxygen fugacity, salt formation temperature) of Mars and Earth. Whereas fine-grained or

375   coarse-grained standards exist for these minerals, we have explored grain sizes that have

376   not previously been studied in reflectance spectroscopy. Spectral modeling of intimate

377   mixtures that include Fe-sulfates has been impossible until now because of the paucity of

378   published optical constants for Fe-sulfates; this study provides optical constants that can

379   be used as inputs to the most commonly used planetary science radiative transfer models.

380   These data will be applicable to a range of studies on evaporate and hydrothermal

381   mineralogy on Mars and useful for designing future Mars sample return missions. These

382   data may also be useful for mapping the abundances and types of Fe-sulfates in terrestrial

383   environments to identify acidic mine water contamination, acidity patterns in

384   groundwater flow, and subsurface mineral resources (Cloutis et al. 2006; Swayze et al.

385   2008).

393   References Cited

394   Anthony, J.W., Bideaux, R.A., Bladh, K.W., and Nichols, M.C., Eds. (2013) Handbook

395   of Mineralogy, Mineralogical Society of America, Chantilly, VA 20151-1110, USA.

396   http://www.handbookofmineralogy.org/, accessed Apr. 18, 2013.

397   Bandfield, J.L. (2002) Global mineral distributions on Mars. Journal of Geophysical

398   Research Planets, 107, 9-1, CiteID 5042, doi:10.1029/2001JE001510.

399   Basciano, L.C., and Peterson, R.C. (2007). Jarosite–hydronium jarosite solid solution

400   series with full iron site occupancy: Mineralogy and crystal chemistry. American

401   Mineralogist, 92, 1464-1473, doi:10.2138/am.2007.2432.

402   Basciano, L.C., and Peterson, R.C. (2008) Crystal chemistry of the natrojarosite-jarosite

403   and natrojarosite-hydronium jarosite solid-solution series: A synthetic study with full

404   Fe site occupancy. American Mineralogist, 93, 853-862.

405   Bibring, J.-P., et al. (2004) OMEGA: Observatoire pour la Mineralogie, l'Eau, les Glaces

406   et l'Activite. In Wilson, A. and Chicarro, A., Eds., Mars Express: the scientific

407   payload, ESA SP-1240, Noordwijk, Netherlands; ESA Publications Division, 37-49.

408   Bibring, J.-P., Langevin, Y., Mustard, J.F., Poulet, F., Arvidson, R., Gendrin, A.,

409   Gondet, B., Mangold, N., Pinet, P., and Forget, F. (2006) Global mineralogical and

410   aqueous Mars history derived from OMEGA/Mars Express data. Science, 312,

411   5772, 400-404.

412   Bishop, J.L., and Murad, E. (1996) Schwertmannite on Mars? Spectroscopic analyses of

413   schwertmannite, its relationship to other ferric minerals, and its possible presence in

414   the surface material on Mars. In M. D. Dyar, C. McCammon, and M. W. Schaefer,

415   Eds., Mineral Spectroscopy: A tribute to Roger G. Burns, Special Publication

416   Number 5, p. 337-358. The Geochemical Society. Houston, TX.

417   Bishop, J.L., and Murad, E. (2005) The visible and infrared spectral properties of jarosite

418   and alunite. American Mineralogist, 90, 1100-1107, doi: 10.2138/am.2005.1700.

419   Bishop, J.L., and Weitz, C.M. (2011) Morphology and mineralogy of light-toned layered

420   deposits on the Juventae Chasma plateau and the location of a proposed future

421   landing site. 42nd Lunar and Planetary Science Conference, 2115.

422   Bishop, J.L., Dyar, M.D., Lane, M.D., and Banfield, J.F. (2004) Spectral identification of

423   hydrated sulfates on Mars and comparison with acidic environments on Earth.

424   International Journal of Astrobiology, 3, 275-285.

425   Bishop, J.L., Lane, M.D., Dyar, M.D., Parente, M., Roach, L.H., Murchie, S.L., and

426   Mustard, J.F. (2008) Sulfates on Mars: how recent discoveries from CRISM,

427   OMEGA, and the MERs are changing our view of the planet. Geochimica et

428   Cosmochimica Acta, 72, A86.

429   Bishop, J.L., Parente, M., Weitz, C.M., Noe Dobrea, E.Z., Roach, L.H., Murchie, S.L.,

430   McGuire, P.C., McKeown, N.K., Rossi, C.M., Brown, A.J., Calvin, W.M., Milliken,

431   R., and Mustard, J.F. (2009) Mineralogy of Juventae Chasma: Sulfates in the light-

432   toned mounds, mafic minerals in the bedrock, and hydrated silica and hydroxylated

433   ferric sulfate on the plateau. Journal of Geophysical Research, 114, E00D09,

434   doi:10.1029/2009JE003352.

435   Blaney, D.L, and McCord, T.B. (1995) Indications of sulfate minerals in the Martian soil

436   from Earth-based spectroscopy. Journal of Geophysical Research, 100, 14,433-

437   14,442.

438   Bridges, J.C., and Grady, M.M. (2000) Evaporite mineral assemblages in the nakhlite

439   (martian) meteorites. Earth and Planetary Science Letters, 176, 267-279.

440   Bridges, J.C., Catling, D.C., Saxton, J.M., Swindle, T.D., Lyon, I.C., and Grady, M.M.

441   (2001) Alteration assemblages in martian meteorites: Implications for near-surface

442   processes. Space Science Reviews, 96, 365-392.

443   Brophy, G.P., and Sheridan, M.F. (1965) Sulfate studies IV: The jarosite- natrojarosite-

444   hydronium jarosite solid solution series. American Mineralogist, 50, 1595-1607.

445   Brown, A.J., Bish, D.L., and Bishop, J.L. (2008) Dehydration of ferrous sulfates

446   monitored by XRD - implications for CHEMIN, Lunar and Planetary Science

447   XXXIX, LPI Contribution No. 1391, p. 1008.

448   Brown, A.J., Bishop, J.L., Roush, T.L., Hunkins, L., Bristow, T., and Blake, D. (2012)

449   Controlled study for quantitative clay abundance on Mars. 43rd Lunar and Planetary

450   Science Conference, 1747.

451   Carter, J., Poulet, F., Bibring, J.-P., Mangold, N., and Murchie, S. (2013) Hydrous

452   minerals on Mars as seen by the CRISM and OMEGA imaging spectrometers:

453   Updated global view. Journal of Geophysical Research: Planets, 118, 831–858,

454   doi:10.1029/2012JE004145.

455   Chatzitheodoridis, E., and Turner, G. (1990) Secondary minerals in the Nakhla

456   meteorite. Meteoritics, 25, 354.

457   Clark, R.N. (1993) SPECtrum processing routines user's manual version 3.0 (program

458   SPECPR). U.S. Geological Survey Open File Report, 93-595, 210 pp.

459   Clark, R.N., Swayze, G.A., Wise, R., Livo, E., Hoefen, T., Kokaly, R., and Sutley, S.J.

460   (2007) USGS digital spectral library splib06a: U.S. Geological Survey, Digital Data

461   Series 231.

462   Cloutis, E.A., Hawthorne, F.C., Mertzman, S.A., Krenn, K., Craig, M.A., Marcino, D.,

463   Methot, M., Strong, J., Mustard, J.F., Blaney, D.L., Bell, J.F. III, and Vilas, F. (2006)

464   Detection and discrimination of sulfate minerals using reflectance spectroscopy.

465   Icarus, 184, 121-157.

466   Cloutis, E.A., Craig, M.A., Mustard, J.F., Kruzelecky, R.V., Jamroz, W.R., Scott, A.,

467   Bish, D.L., Poulet, F., Bibring, J.-P., and King, P.L. (2007) Stability of hydrated

468   minerals on Mars. Geophysical Research Letters, 34, CiteID L20202,

469   doi:10.1029/2007GL031267.

470   Cloutis, E.A., Craig, M.A., Kruzelecky, R.V., Jamroz, W.R., Scott, A., Hawthorne, F.C.,

471   and Mertzman, S.A. (2008) Spectral reflectance properties of minerals exposed to

472   simulated Mars surface conditions. Icarus, 195, 140-168.

473   Cooper, C.D., and Mustard, J.F. (2002) Spectroscopy of loose and cemented sulfate-

474   bearing soils: implications for duricrust on Mars. Icarus, 158, 42-55.

475   Craig, M., Cloutis, E.A., Kaletzke, L., McCormack, K., and Stewart, L. (2006) Alteration

476   of hydration absorption features in reflectance spectra of selected sulfates in a low

477   pressure environment; 0.45-4.3 µm. Lunar and Planetary Science Conference

478   XXXVII, 2112.

479   Dalton, J.B. III, and Pitman, K.M. (2012) Low temperature optical constants of some

480   hydrated sulfates relevant to planetary surfaces. Journal of Geophysical Research:

481   Planets, 117, CiteID E09001, doi:10.1029/2011JE004036.

482   Dyar, M.D., Lane, M.D., Bishop, J.L., O'Connor, V., Cloutis, E., and Hiroi, T. (2005)

483   Integrated spectroscopic studies of hydrous sulfate minerals. Lunar and Planetary

484   Science Conference XXXVI, 1622.

485   Fairen, A.G., Schulze-Makuch, D., Rodriguez, A.P., Fink, W., Davila, A.F., Uceda, E. R.,

486   Furfaro, R., Amils, R., and McKay, C.P. (2009) Evidence for Amazonian acidic

487   liquid water on Mars – a reinterpretation of MER mission results. Planetary and

488   Space Science, 57, 276-287.

489   Farquhar, J., Kim, S.-T., and Masterson, A. (2007) Implications from sulfur isotopes of

490   the Nakhla meteorite for the origin of sulfate on Mars. Earth and Planetary Science

491   Letters, 264, 1-8.

492   Farrand, W.H., Rice, J.W., and Glotch, T.D. (2009) Evidence of the presence of jarosite

493   and diagenetic activity in the Mawrth Vallis region. Lunar and Planetary Science

494   Conference XL, 2080.

495   Folk, R.L. (1974) Petrology of sedimentary rocks: Austin, Texas, Hemphill Publishing

496   Company, 182 pp. http://www.lib.utexas.edu/geo/folkready/

497   Freeman, J.J., and Wang, A. (2009) Hydrated magnesium sulfates below 0°C – stable

498   phases and polymorphs. Lunar and Planetary Science Conference XL, 2301.

499   Freeman, J.J., Jin, M., and Wang, A. (2008) D_2O substitution experiment on hydrated

500   iron and magnesium sulfates and its application for spectral interpretation of martian

501   sulfates. Lunar and Planetary Science Conference XXXIX, 2390.

502   Gendrin, A., Mangold, N., Bibring, J.-P., Langevin, Y., Gondet, B., Poulet, F.,

503   Bonello, G., Quantin, C., Mustard, J., Arvidson, R., and LeMouélic, S. (2005)

504   Sulfates in martian layered terrains: The OMEGA/Mars Express view. Science 307,

505   5715, 1587-1591.

506   Golden, D.C., Ming, D.W., Morris, R.V., and Mertzman, S.A. (2005) Laboratory-

507   simulated acid-sulfate weathering of basaltic materials: implications for formation of

508   sulfates at Meridiani Planum and Gusev crater, Mars. Journal of Geophysical

509   Research, 110(E12), CiteID E12S07.

510   Gooding, J.L. (1992) Soil mineralogy and chemistry on Mars – possible clues from salts

511   and clays in SNC meteorites. Icarus, 99, 28-41.

512   Hapke, B.W. (1993) Theory of reflectance and emittance spectroscopy. Cambridge Univ.

513   Press, New York.

24

514   Hapke, B. (2002) Bidirectional reflectance spectroscopy 5. The coherent backscatter

515   opposition effect and anisotropic scattering. Icarus, 157, 523–534,

516   doi:10.1006/icar.2002.6853.

517   Hapke, B.W. (2008) Bidirectional reflectance spectroscopy. Icarus, 195, 918-926.

518   Johnson, J.R., Bell, J.F., Cloutis, E., Staid, M., Farrand, W.H., McCoy, T., Rice, M.,

519   Wang, A., and Yen, A. (2007) Mineralogic constraints on sulfur-rich soils from

520   Pancam spectra at Gusev Crater, Mars. Geophysical Research Letters, 34, L13202,

521   doi:10.1029/2007GL029894.

522   Kieffer, H.H., Jakosky, B.M., Snyder, C.W., and Matthews, M.S., Eds. (1992) Mars,

523   University of Arizona Press (Tucson, AZ), 1498 pp.

524   King, P.L., and McSween, H.Y. (2005) Effects of H_2O, pH, and oxidation state on the

525   stability of Fe minerals on Mars. Journal of Geophysical Research, 110(E12),

526   CiteID E12S10.

527   Lichtenberg, K.A., Arvidson, R.E., Morris, R.V., Murchie, S.L., Bishop, J.L.,

528   Fernandez Remolar, D., Glotch, T.D., Noe Dobrea, E., Mustard, J.F., Andrews-Hanna, J.,

529   and Roach, L.H. (2010) Stratigraphy of hydrated sulfates in the sedimentary

530   deposits of Aram Chaos, Mars.   Journal of Geophysical Research, 115(B6),

531   E00D17.

532   Lane, M.D., Dyar, M.D., and Bishop, J.L. (2004) Spectroscopic evidence for hydrous

533   iron sulfate in the Martian soil. Geophysical Research Letters, 31, CiteID L19702,

534   doi:10.1029/2004GL021231.

535   Lane, M.D., Bishop, J.L., Dyar, M.D., King, P.L., Parente, M., and Hyde, B.C. (2008)

536   Mineralogy of the Paso Robles soils on Mars. American Mineralogist, 93, 728-739.

537   Ling, Z.C., and Wang, A. (2010) A systematic spectroscopic study of eight hydrous ferric

538   sulfates relevant to Mars. Icarus, 209, 422–433.

539   Liu, Y., and Wang, A. (2012) Dehydration of Na-jarosite, ferricopiapite, and

540   rhomboclase at high T and implications on martian ferric sulfates. 43rd Lunar and

541   Planetary Science Conference, 2791.

542   Lucey, P.G. (1998) Model near-infrared optical constants of olivine and pyroxene as a

543   function of iron content. Journal of Geophysical Research, 103, 1703-1713.

544   Marion, G.M., and Farren, R.E. (1999) Mineral solubilities in the Na-K-Mg-Ca-Cl-SO$_4$-

545   H$_2$O system: a re-evaluation of the sulfate chemistry in the Spencer-Moller-Weare

546   model. Geochimica et Cosmochimica Acta, 63, 1305-1318.

547   Moersch, J.E., and Christensen, P.R. (1995) Thermal emission from particulate surfaces:

548   a comparison of scattering models with measured spectra. Journal of Geophysical

549   Research, 100(E4), 7465-7477.

550   Morris, R.V., Golden, D.C., Ming, D.W., Graff, T.G., Arvidson, R.E., Wiseman, S.M.,

551   Lichtenberg, K.A., and Cull, S. (2009) Visible and near-IR reflectance spectra for

552   smectite, sulfate and perchlorate under dry conditions for interpretation of martian

553   surface mineralogy. Lunar and Planetary Science Conference XL, 2317.

554   Murchie, S., Arvidson, R., Bedini,, P., Beisser, K., Bibring,, J.-P., Bishop, J., Boldt, J.,

555   Cavender,, P., Choo,, T., Clancy, R.T., Darlington, E.H., Des Marais, D., Espiritu,

556   R., Fort, D., Green, R., Guinness, E., Hayes, J., Hash, C., Heffernan, K.,

557   Hemmler, J., Heyler, G., Humm, D., Hutcheson, J., Izenberg, N., Lee, R., Lees, J.,

558   Lohr, D., Malaret, E., Martin, T., McGovern, J.A., McGuire, P., Morris, R.,

559   Mustard, J., Pelkey, S., Rhodes, E., Robinson, M., Roush, T., Schaefer, E.,

560   Seagrave, G., Seelos, F., Silverglate, P., Slavney, S., Smith, M., Shyong, W.-J.,

561   Strohbehn, K., Taylor, H., Thompson, P., Tossman, B., Wirzburger, M., and

562   Wolff, M. (2007) Compact Reconnaissance Imaging Spectrometer for Mars

563   (CRISM) on Mars Reconnaissance Orbiter (MRO). Journal of Geophysical

564   Research, 112, CiteID E05S03.

565 Murchie, S.L., Mustard, J.F., Ehlmann, B.L., Milliken, R.E., Bishop, J.L., McKeown,

566   N.K., Noe Dobrea, E.Z., Seelos, F.P., Buczkowski, D.L., Wiseman, S.M., Arvidson,

567   R.E., Wray, J.J., Swayze, G.A., Clark, R.N., Des Marais, D.J., McEwen, A.S., and

568   Bibring, J.P. (2009) A synthesis of Martian aqueous mineralogy after 1 Mars year of

569   observations from the Mars Reconnaissance Orbiter. Journal of Geophysical

570   Research, 114, doi:10.1029/2009JE003342.

571 Pelkey, S.M., Mustard, J.F., Murchie, S., Poulet, F., Bibring, J.-P., Bishop, J., Izenberg,

572   N., Seelos, F., Ehlmann, B.L., Roach, L.H., Milliken, R.E., and the

573   CRISM Science Team (2007) CRISM observations of hydrated craters deposits in

574   Terra Tyrrhena, Mars. Lunar and Planetary Science Conference XXXVIII, 1994.

575 Pitman, K.M., Wolff, M.J., and Cloutis, E.A. (2013) Radiative transfer in clusters of

576   regolith particles: fundamental scattering unit? Lunar and Planetary Science

577   Conference XLIV, 2337.

578 Pollack, J.B., Roush, T.L., Witteborn, F., Bregman, J., Wooden, D., Stoker, C., Toon, O.

579   B., Rank, D., Dalton, B., and Freedman, R. (1990) Thermal emission spectra of

580   Mars (5.4 - 10.5 µm): evidence for sulfates, carbonates and hydrates. Journal of

581   Geophysical Research, 95, 14595-14627.

27

582   Ramsey, M.S., and Christensen, P.R. (1998) Mineral abundance determination:

583   quantitative deconvolution of thermal emission spectra. Journal of Geophysical

584   Research, 103, 577-596.

585   Roach, L.H., Mustard, J., Gendrin, A., Fernández-Remolar, D., Amils, R., and Amaral-

586   Zettler, L. (2006) Finding mineralogically interesting targets for exploration from

587   spatially coarse visible and near IR spectra. Earth and Planetary Science Letters,

588   252, 201–214.

589   Roach, L.H., Mustard, J.F., Lane, M.D., Bishop, J.L., and Murchie, S.L. (2010)

590   Diagenetic haematite and sulfate assemblages in Valles Marineris. Icarus, 207, 659-

591   674.

592   Rothstein, Y.R., Dyar, M.D., and Bishop, J.L. (2006) Moessbauer and reflectance

593   spectroscopy of synthetic jarosite with variable compositions and temperatures,

594   Lunar and Planetary Science Conference XXXVII, 1727.

595   Roush, T.L., Brown, A.J., Bishop, J., Blake, D., and Bristow, T.F. (2013) Initial

596   estimates of optical constants of Mars candidate materials, 44th Lunar and Planetary

597   Science Conference, LPI Contribution No. 1719, p. 1297.

598   Shkuratov, Y., Starukhina, L., Hoffmann, H., and Arnold, G. (1999) A model of spectral

599   albedo of particulate surfaces: Implications for optical properties of the Moon.

600   Icarus, 137, 235-246.

601   Sklute, E.C., Glotch, T.D., and Dyar, M.D. (2012) VNIR optical constant determination

602   of synthetic jarosites for quantitative abundance analysis of remote sensing data sets,

603   43rd Lunar and Planetary Science Conference, 1508.

604   Sklute, E.C., Glotch, T.D., and Woerner, W. (2013) Visible and near infrared optical

605   constants of synthetic jarosites. 44th Lunar and Planetary Science Conference, 2142.

606   Spratt, H.J., Rintoul, L., Avdeev, M., and Martens, W.N. (2013) The crystal structure and

607   vibrational spectroscopy of jarosite and alunite minerals, American Mineralogist, 98,

608   1633-1643.

609   Squyres, S.W., Grotzinger, J.P., Arvidson, R.E., Bell, J.F. III, Calvin, W. Christensen, P.

610   R., Clark, B.C., Crisp, J.A., Farrand, W.H., Herkenhoff, K.E., Johnson, J.R.,

611   Klingelhöfer, G., Knoll, A.H., McLennan, S.M., McSween, H.Y., Morris, R.V.,

612   Rice, J.W., Rieder, R., and Soderblom, L.A. (2004) In situ evidence for an ancient

613   aqueous environment at Meridiani Planum, Mars. Science, 306, 5702, 1709-1714.

614   Swayze, G.A., Desborough, G.A., Smith, K.S., Lowers, H.A., Hammarstrom, J.M.,

615   Diehl, S.F., Leinz, R.W., and Driscoll, R.L. (2008) Chapter B: Understanding

616   jarosite – from mine waste to Mars, p. 8-13. In Verplanck, P. L., Ed..

617   Understanding contaminants associated with mineral deposits: U.S. Geological

618   Survey Circular 1328, 96 pages.

619   Tosca, N.J., McLennan, S.M., Dyar, M.D., Sklute, E.C., and Michel, F.M. (2008) Fe

620   oxidation processes at Meridiani Planum and implications for secondary Fe

621   mineralogy on Mars. Journal of Geophysical Research, 113(E5), CiteID E05005.

622   Toulmin, P., Baird, A.K., Clark, B.C., Keil, K., Rose, H.J., Jr., Christian, R.P., Evans, P.

623   H., and Killiher, W.C. (1977) Geochemical and mineralogical interpretation of the

624   Viking inorganic chemical results. Journal of Geophysical Research, 84, 4625-4634.

625   Treiman, A.H. (1993) The parent magma of the Nakhla (SNC) meteorite, inferred from

626   magmatic inclusions. Geochimica et Cosmochimica Acta, 57, 4753.

627   Wang, A., and Ling, Z.C. (2011) Ferric sulfates on Mars: A combined mission data

628   analysis of salty soils at Gusev crater and laboratory experimental investigations,

629   Journal of Geophysical Research, 116, E00F17, doi:10.1029/2010JE003665.

630   Warren, S.G. (1984) Optical constants of ice from the ultraviolet to the microwave.

631   Applied Optics, 23, 1206-1225.

632   Weitz, C.M., Williams, R., Noe Dobrea, E., and Baldridge, A. (2012) Hydrated minerals

633   and fluvial features in and around the Melas Chasma basin. 43rd Lunar and Planetary

634   Science Conference, 2304.

635   Weitz, C.M., Noe Dobrea, E., and Wray, J.J. (2013) Gypsum, jarosite, and other minerals

636   associated with a blocky deposit in western Melas Chasma, 44th Lunar and Planetary

637   Science Conference, 2076.

638   Wentworth, S.J., Thomas-Keprta, K.L., and McKay, D.S. (2002) Water on Mars:

639   petrographic evidence. Lunar and Planetary Science XXXIII, 1932.

640   Wentworth, S.J., Gibson, E.K., Velbel, M.A., and McKay, D.S. (2005) Antarctic dry

641   valleys and indigenous weathering in Mars meteorites: implications for water and

642   life on Mars. Icarus, 174, 383-395.

643   Vaniman, D.T., Bish, D.L., Chipera, S.J., Fialips, C.I., Carey, J.W., and Feldman, W.C.

644   (2004) Magnesium sulphate salts and the history of water on Mars. Nature, 431,

645   663.

646   Weitz, C.M., Noe Dobrea, E.Z., Williams, R.M.E., Metz, J., Quantin, C., Parente, M.,

647   and Grotzinger, J. (2009) MRO observations of fluvial features, sulfates, and other

648   landforms in the Melas Chasma basin. Lunar and Planetary Science Conference XL,

649   1874.

30

650   Wray, J.J., Milliken, R.E., Swayze, G.A., Dundas, C.M., Bishop, J.L., Murchie, S.L.,

651   Seelos, F.P., and Squyres, S.W. (2009a) Columbus Crater and other possible

652   paleolakes in Terra Sirenum, Mars. Lunar and Planetary Science Conference XL,

653   1896.

654   Wray, J.J., Noe Dobrea, E.Z., Arvidson, R.E., Wiseman, S.M., Squyres, S.W., McEwen,

655   A.S., Mustard, J.F., and Murchie, S.L. (2009b) Phyllosilicates and sulfates at

656   Endeavour Crater, Meridiani Planum, Mars. Geophysical Research Letters, 36,

657   L21201, doi:10.1029/2009GL040734.

658   Wray, J.J., Murchie, S.L., Squyres, S.W., Seelos, F.P., and Tornabene, L.L. (2009c)

659   Diverse aqueous environments on ancient Mars revealed in the southern highlands.

660   Geology, 37, 1043-1046, doi: 10.1130/G30331A.1.

661   Yang, W.-C. (2003) Handbook of Fluidization and Fluid-Particle Systems Ebook

662   Library, Ebooks Corporation CRC Press, Marcel Dekker Ltd., 1868 pages.

663

664

665

666

667

668

669

670

671

672

673　**Table 1.** Examples of prior Mars-relevant reflectance spectral studies of Fe-sulfates

Mineral Name	Wavelength Range (µm)	Temperature (K)	Particle Size (µm)	Source
Szomolnokite, jarosite, ferriocopiapite, coquimbite, schwertmannite	0.35-5; 5-25	Not specified	< 45, < 125	Lane et al. (2004); Bishop and Murad (1996); Bishop et al. (2004)
Fe- & Mg-sulfates, e.g., szomolnokite, melanterite	0.3-5	Not specified (Mars conditions)	< 45 (<125 szomolnokite only)	Dyar et al. (2005)
Jarosite	0.2-5.3; 0.3-25	300	< 45	Bishop and Murad (2005); Rothstein et al. (2006); Clark et al. (2007)
42 Fe- & Mg-sulfates (Mars conditions)	0.45-4.3; 0.3-26	293.15	< 45	Craig et al. (2006); Cloutis et al. (2006, 2008); HOSERLab (2013)
Jarosite; hydronium jarosite	1.2-2.6	Not specified	Not specified	Basciano & Peterson (2007)
Jarosite (K-, Na-, hydronium)	0.35-2.5	Not specified	Not specified	Swayze et al. (2008)
Melanterite (Mars conditions)	0.35-2.5	~300; <273.15 (263.15)	Not specified	Freeman et al. (2008); Freeman and Wang (2009)
Melanterite, szomolnokite, ferric sulfate hydroxide (Mars conditions)	0.35-2.5	298.15 25 °C, 50-330 °C; Humid (laboratory air) and dry (dry N_2 gas) environments	Not specified	Morris et al. (2009)
Ferricopiapite, rhomboclase, kornelite, pentahydrate, ferric sulfate, etc.	0.35-2.5	Not specified	Not specified	Wang & Ling (2011) and references therein
Na-jarosite, rhomboclase, ferricopiapite	0.4-2.5	50 & 95 °C for dehydration; ambient	Not specified	Liu & Wang (2012)
Synthetic jarosite	0.35-2.5; 0.9-4.76; 1.6-28.5	ambient	< 45, 45-125, 125-180; < 63, 63-90, 90-125	Sklute et al. (2012, 2013)
K-, Na-, synthesized jarosites;	0.35-2.5	ambient	< 45; < 125	PDS Geosciences Node (2013)

ferricopiapite, coquimbite, szomolnokite, rozenite, romerite, amaranthine				
K-, Na-, Pb-jarosite	0.4-2.5; 2-15.385	ambient	< 45; 45-125; 125-500	ASTER (2013)
Jarosite; natrojarosite	0.32-2.55	ambient; 300, 248 °C	< 25, 25-75, 75-150, < 45, 125-1000, < 125, < 500, < 75; < 45, 45-125, > 125	RELAB (2013)
Rhomboclase		ambient	45, < 50, < 125, < 250, 45-125, 125-250	
Szomolnokite		ambient	< 45, 45-125, < 125, > 125	
Coquimbite		ambient	< 125, < 45, 125-500, < 75	
Copiapite; ferricopiapite		ambient	< 25, 25-75, 75-150, <45, < 125, 45-125, 125-250, 250-1000, < 75; < 45, < 125	

674

675 **Table 2.** Samples used in this study

Mineral Name	Description	Structural formula	Source
Jarosite	Potassium iron sulfate hydroxide	$KFe^{3+}_3(SO_4)_2(OH)_6$	(1) Copiapo Jarosite Mine, Dona Ana Co., New Mexico, U. S. A. (2) Arabia District, Pershing County, Nevada, U. S. A. (3) Grande Lode, La Colorado Mine, Cercado Province, Oruro, Bolivia
Natrojarosite	Sodium iron sulfate hydroxide	$NaFe^{3+}_3(SO_4)_2(OH)_6$	Natural sample from Caltech collection; source unknown
Rhomboclase		$H_5Fe^{3+}O_2(SO_4)_2 \cdot 2H_2O$	Alcaparrosa, Chile
Szomolnokite	Monohydrated iron sulfate	$Fe^{2+}SO_4 \cdot H_2O$	Synthesized

676

677   **Table 3.** Grain sizes used to derive n, k

Mineral	Sieve Interval	Median of Range	Weighted Mean Diameter[1]	Microscopy Diameter[2]		Diameter Used (μm)
			Initial Estimates (μm)	**Mode 1**	**Mode 2** (e.g., fines)	
Jarosite (Copiapo)	53-75	64	89.79	56.67 ± 38.52	6.64 ± 5.93	57
	75-106	90.5	112.55	104.15 ± 25.01	6.00 ± 3.69	104
	106-125	115.5	128.68	135.54 ± 22.14	7.54 ± 6.04	135
	125-150	137.5	158.50	170.44 ± 24.36	~5 ± 4	170
	150-224	187	240.13	244.27 ± 50.22	5.19 ± 1.27	244
	224-250	237	296.40	296.37 ± 42.17	~4 ± 2	296
Jarosite (Arabia)			72.64	33.97 ± 8.52 75.83 ± 19.43	7.75 ± 3.18,	76
			128.45	51.67 ± 15.35, 113.53 ± 13.63	9.23 ± 8.03	Excluded
			128.92	133.35 ± 38.53	9.94 ± 8.13	133
			186.14	~135 ± 20, 188.50 ± 12.35, 266.75 ± 8.77	~15 ± 10, 49.62±15.30	Excluded
			247.30	249.60 ± 54.59	19.34±14.45	250
			319.38	319.22 ± 37.17	~20 ± 12	319
Natrojarosite			104.23	87.94 ± 26.96	10.94 ± 7.42	88
			152.95	121.02 ± 53.55	16.21 ± 4.74	121
			179.85	148.78 ± 36.02	13.85 ± 8.75	149
			200.36	142.60 ± 73.25	~10 ± 10	143
			235.61	213.42 ± 53.75	4.90 ± 1.91	213
			281.68	286.83 ± 82.28	15.60±12.62	287
Rhomboclase			---	---	---	64
			---	---	---	90.5
			153.85	152.91 ± 28.42	5.65 ± 0.52	153
			183.40	156.58 ± 62.05	16.33 ± 5.02	157
			278.07	247.81 ± 75.55	14.98 ± 8.74	248
			325.43	298.23 ± 52.65	186.97 ± 45.48	298
Szomolnokite			69.57	57.20 ± 21.57	~8.5 ± 5	57
			114.87	88.06 ± 28.61	7.48 ± 4.00	88
			133.14	133.12 ± 18.34	10.56 ± 6.55	133
			146.24	145.14 ± 45.59	11.14 ± 8.63	145
			277.11	222.91 ± 36.27	12.39±11.69	223
			284.71	302.92 ± 36.41	13.01±11.76	303

678   Notes:

679   [1]Roush (2005), page 260. [2]Mean and standard deviation values from a Gaussian histogram fit. Duplicated

680   or poorly sorted grain sizes were excluded from n, k derivation.

681

682 **Table 4.** Refractive index assumptions[1] for n_{vis}

Unixial (-)	n_ω	n_ε		n_vis
Jarosite	1.791 – 1.820	1.705 – 1.715		1.760
	1.815 – 1.820	*1.713 – 1.715*		
Natrojarosite	1.832	1.750		1.790
	1.830			
Biaxial (+)	n_α	n_β	n_γ	n_vis
Rhomboclase	1.534	1.553 – 1.555	1.634 – 1.638	1.575
Szomolnokite	1.591	1.623	1.663	1.626

683 Notes:

684 [1]Table values adopted from Anthony et al. (2013), http://www.webmineral.com, http://www.mindat.org.
685

686 **(a)**   **(b)**

687
688
689 **(c)**   **(d)**
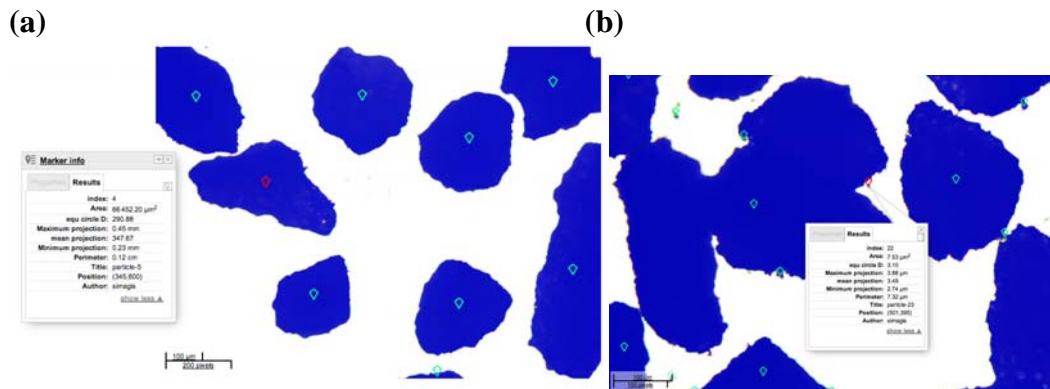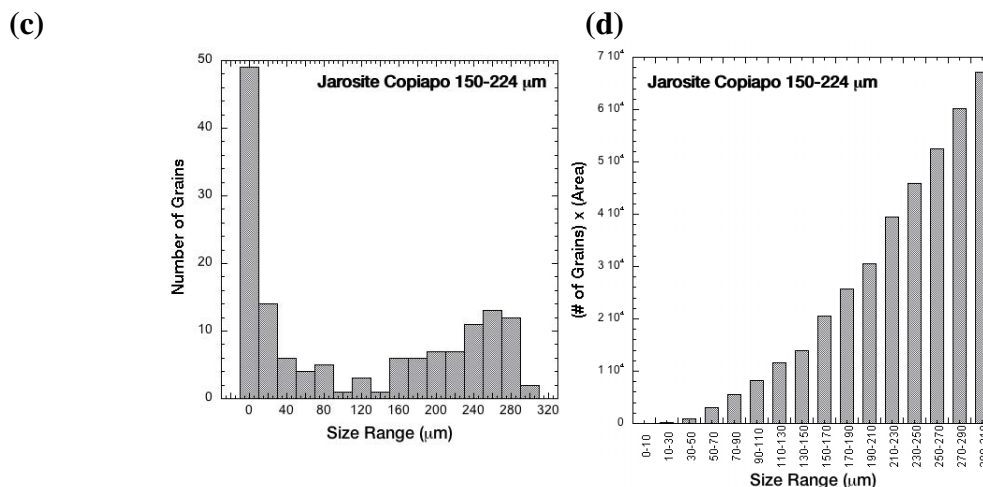
690
691
692 **Figure 1.** Example of diameter determination from optical microscopy images

693 using Simagis Live™ particle size analysis software. Panel (a): one field-of-view for K-

694 jarosite (Copiapo Mine) d_{sieve} = 150-224 μm size fraction. Panel (b): The minimum grain

695 size in this size fraction (the "0th" bin of panel c right histogram) is 3.1 μm. Panels (c, d):

696 Histograms represent total results for eight fields-of-view. The left histogram illustrates

697   the number of grains in each d_{sieve} size bin ("mode 2" given in Table 3). The right

698   histogram scales the number of grains per size bin by geometric cross-sectional area

699    $\pi(d/2)^2$, to yield the dominant grain size affecting area (Table 3 "mode 1").
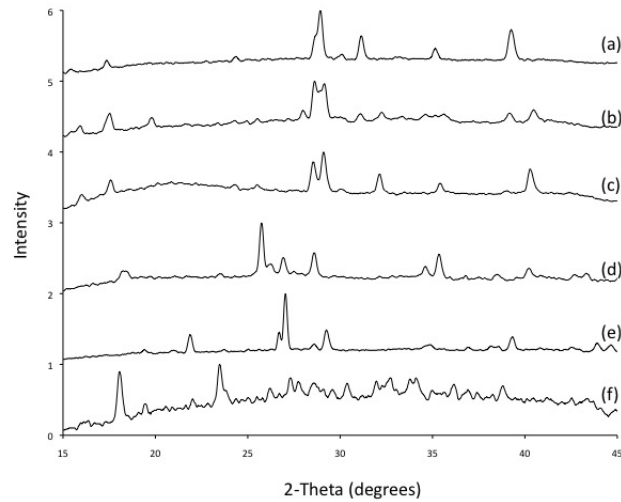
700
701   **Figure 2.** X-ray diffraction patterns for Fe-sulfates: (a) jarosite, (b) jarosite +

702   natrojarosite, (c) natrojarosite, (d) szomolnokite, (e) rhomboclase, and (f) melanterite.

703   The intensity of each pattern has been normalized to 1 and offset by 1 for clarity.

704

705

706

707

708

709

710

711

712

713

714   **(a)**   **(b)**

715

716   **(c)**   **(d)**

717
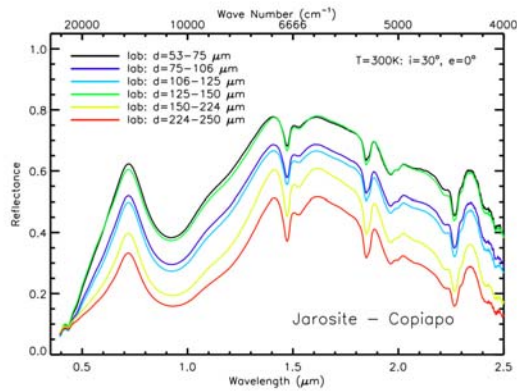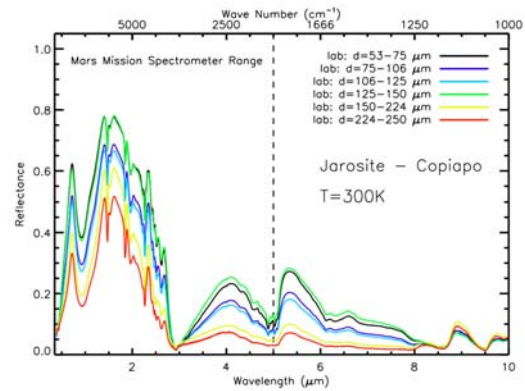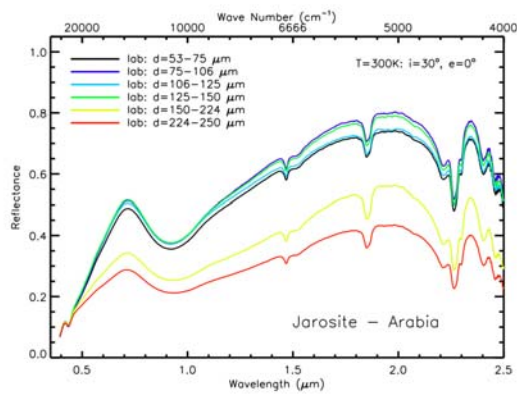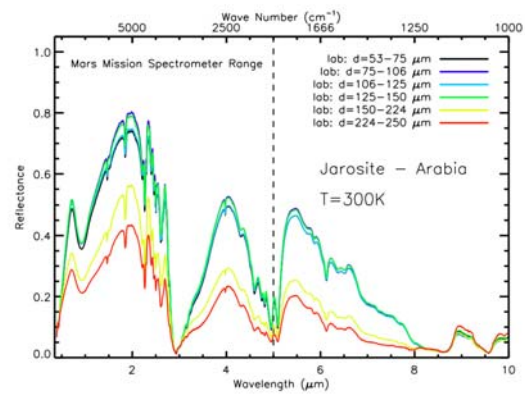
718   **(e)**
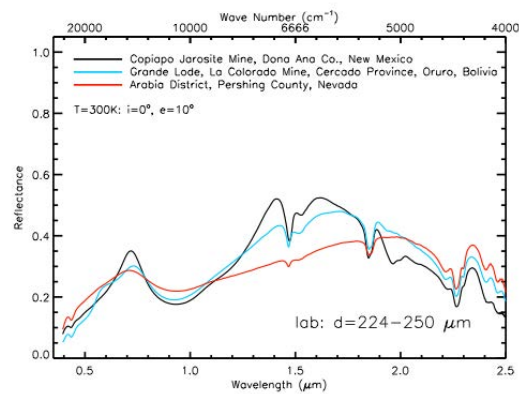
719

720   **Figure 3.** Jarosite laboratory diffuse reflectance spectra in six grain sizes.

721   Panel (a, b): K-jarosite and Na- and/or H_3O^+-jarosite with a hydrated mineral

722   contaminant, from Copiapo Jarosite Mine, Dona Ana County, New Mexico. The band at

723   1.9 µm is not diagnostic of K-jarosite but due to either hydronium or a hydrated

724   component (cf. water band "B" in synthetic K-jarosite, figure 11, Basciano & Peterson

725   2007). Panel (c, d): Pure K-jarosite, from Arabia District, Pershing County, Nevada.

726   Panel (e) illustrates the spectral differences between natural jarosite from three localities.

727

728   **(a)**   **(b)**

729

730   **(c)**   **(d)**

731
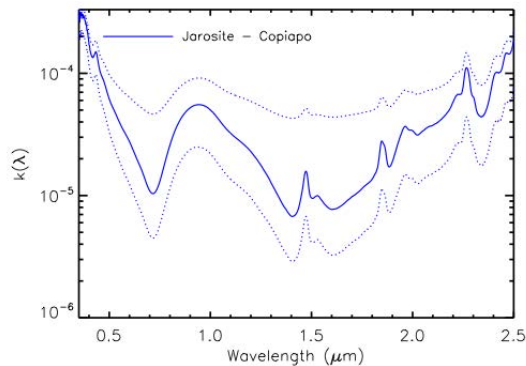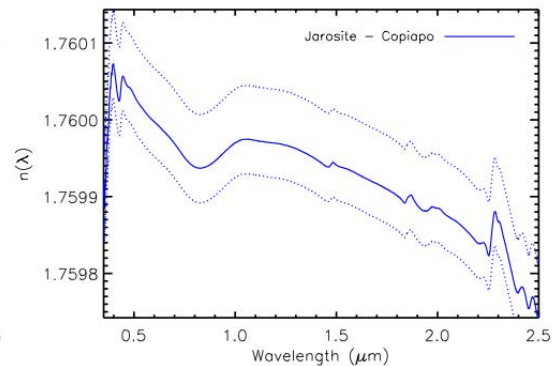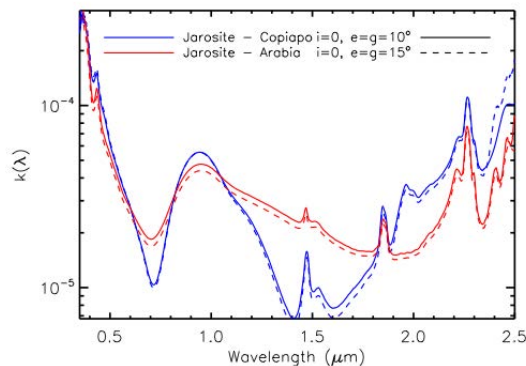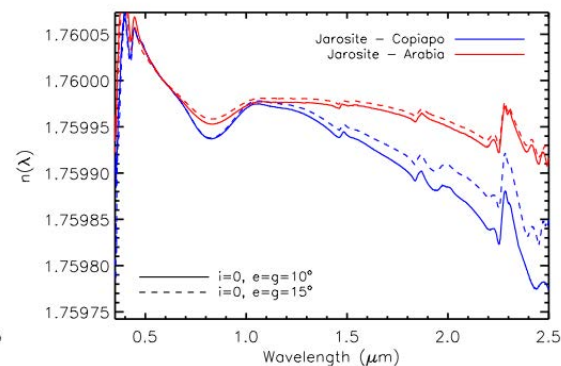
732   **Figure 4.** K-jarosite imaginary and real indices of refraction $k(\lambda)$ and $n(\lambda)$, for

733   Copiapo Mine and Arabia samples. Top panels: dotted lines indicate estimated error

734   bars. Bottom panels: solid vs. dashed lines illustrate the effect of viewing angle on

735   average indices of refraction. Colored lines indicate the differences in optical constants

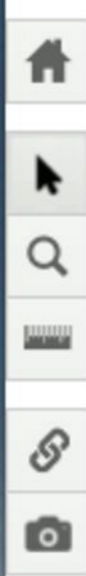736   due to spectral differences of the natural K-jarosite samples.

737 **(a)** **(b)** **(c)**

738

739 **(d)** **(e)** **(f)**

740

741 **(g)** **(h)** **(i)**

742
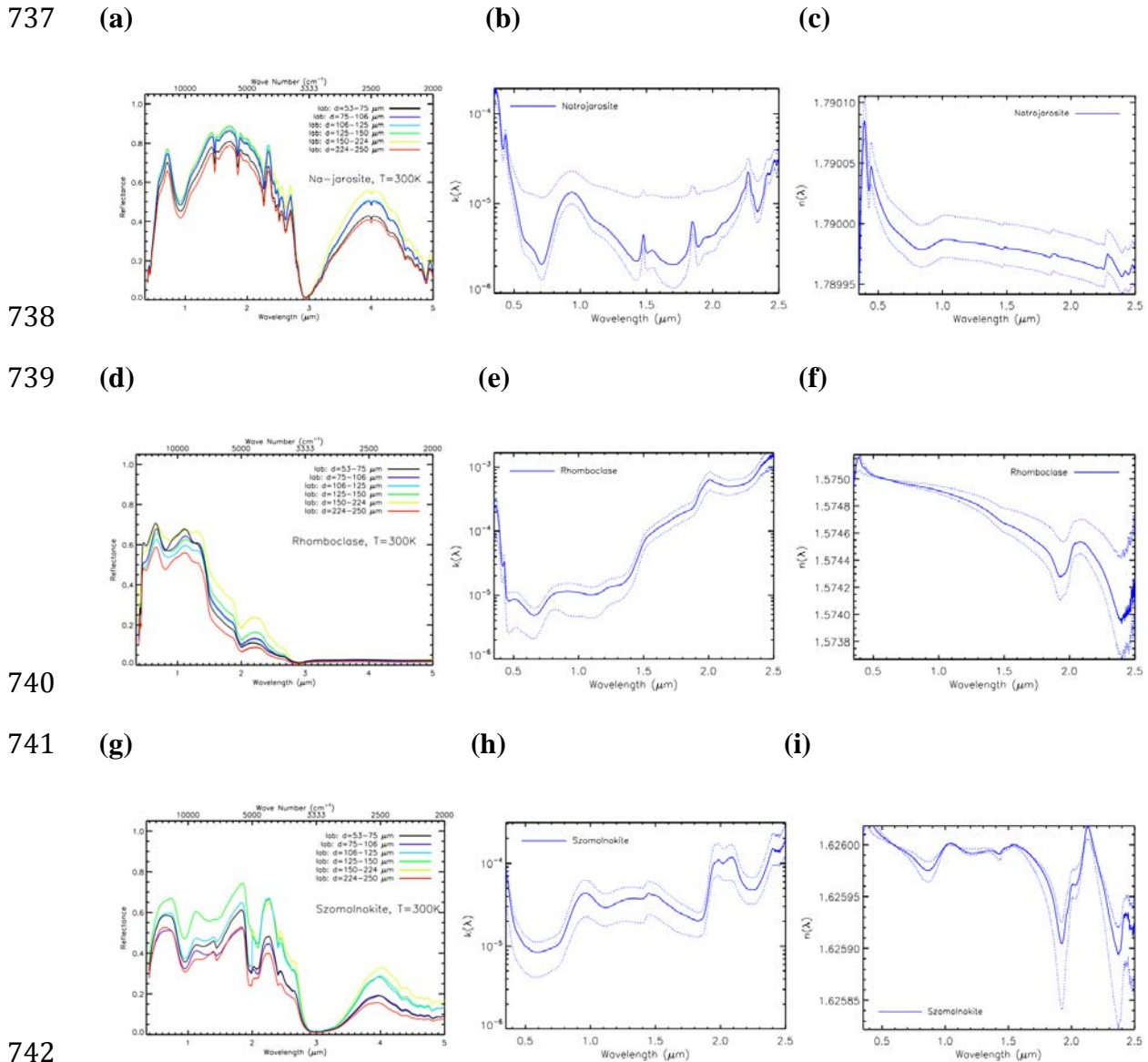
743 **Figure 5.** Na-jarosite (panels a-c), rhomboclase (panels d-f), and szomolnokite

744 (panels g-i) diffuse reflectance spectra and optical constants $k(\lambda)$ and $n(\lambda)$. Dashed lines

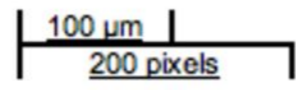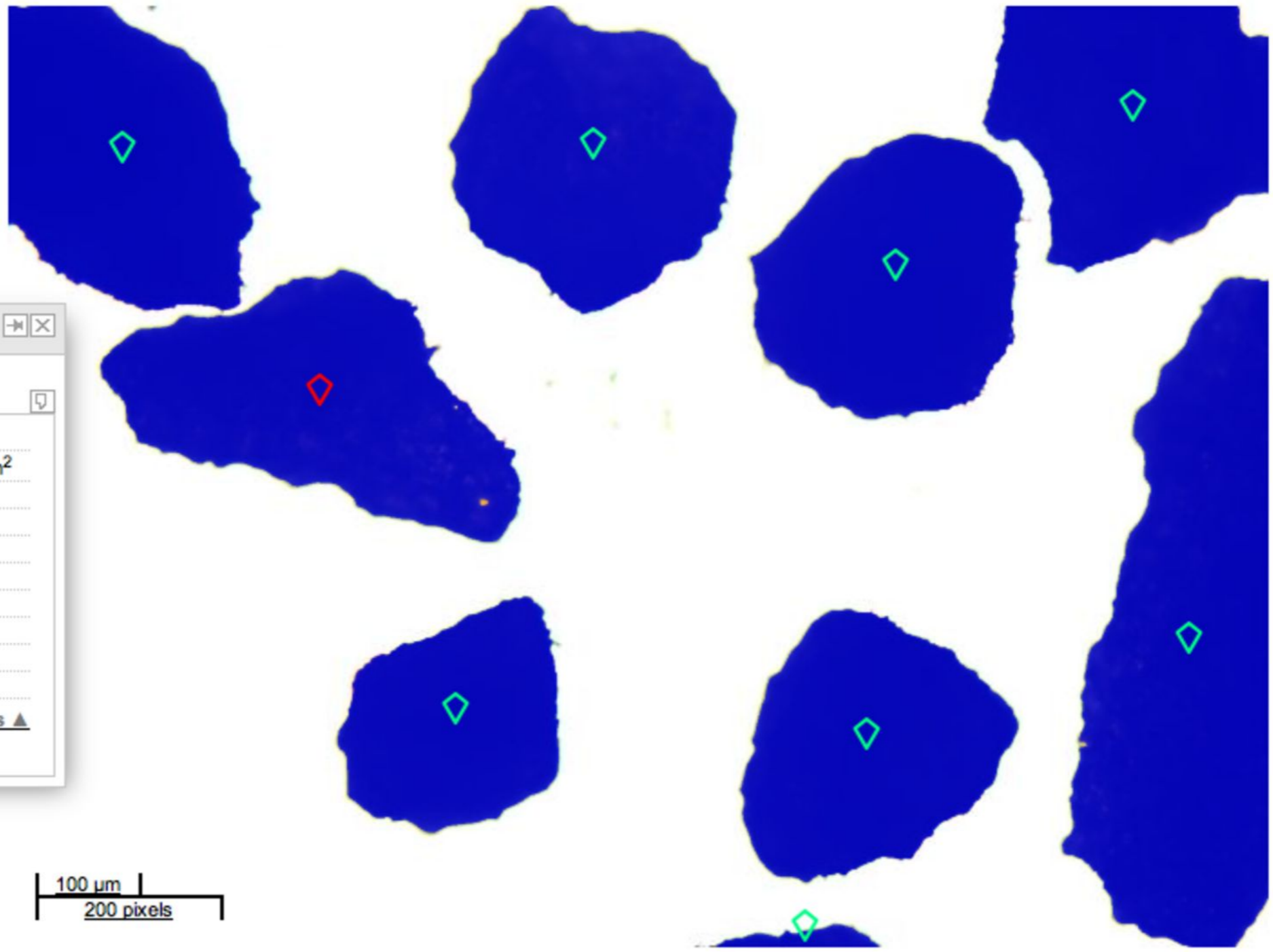745 represent upper and lower bounds on estimated $k(\lambda)$ and $n(\lambda)$.

746

b.jpg

Marker info

Properties | **Results**

index:	4
Area:	66 452.20 μm²
equ circle D:	290.88
Maximum projection:	0.45 mm
mean projection:	347.67
Minimum projection:	0.23 mm
Perimeter:	0.12 cm
Title:	particle-5
Position:	(345,600)
Author:	simagis

show less ▲

100 μm
200 pixels

Jarosite_Copiano_150-224▲
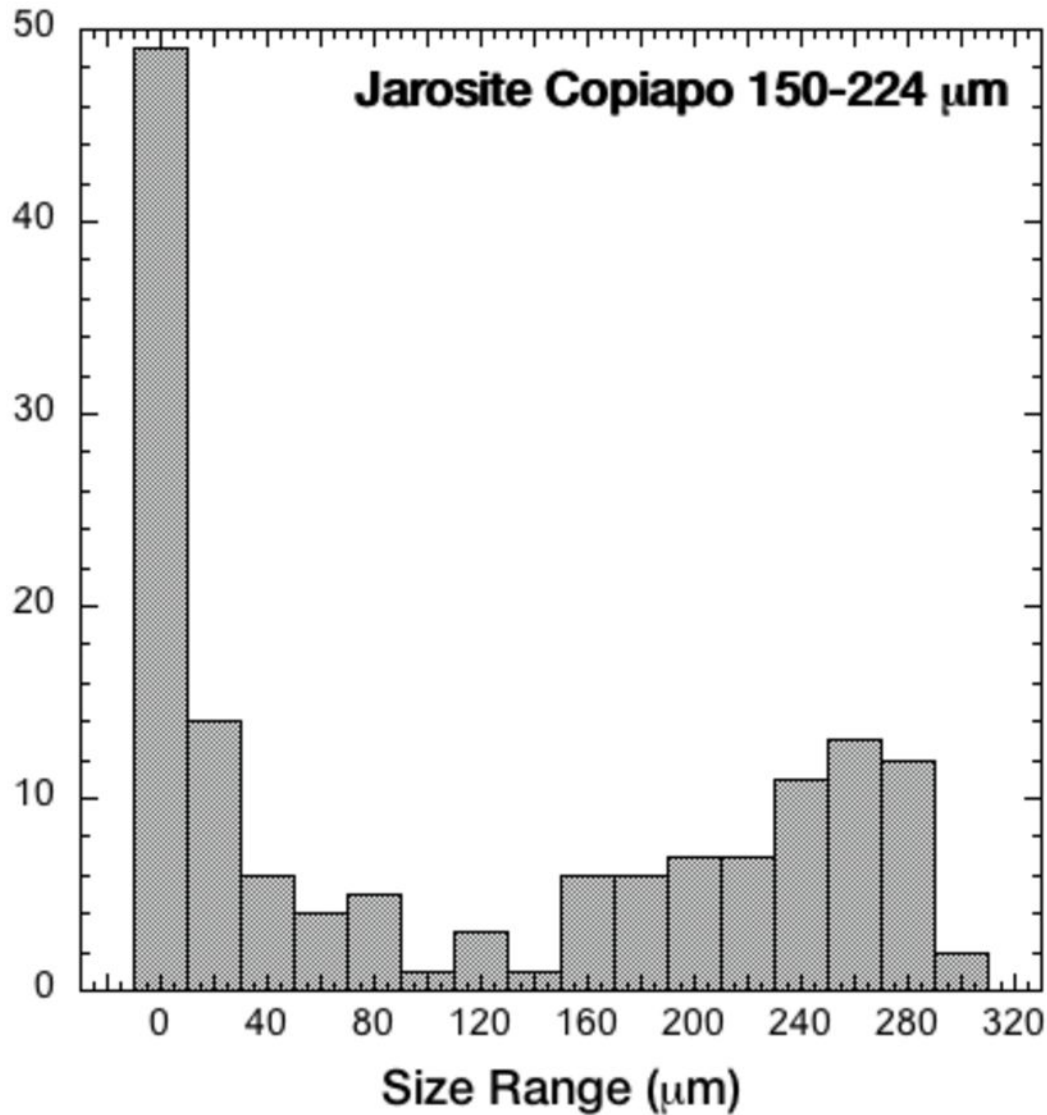
1px = 0.91464μm | Coords: 597, -216 pixels 546.0, -197.6 μm | **Drag to navigate, Shift+drag to select markers** | karpitman | Powered by **Simagis Live™**

Jarosite Copiapo 150-224 μm

Jarosite Copiapo 150–224 μm

Na-jarosite, T=300K

lab: d=53−75 μm
lab: d=75−106 μm
lab: d=106−125 μm
lab: d=125−150 μm
lab: d=150−224 μm
lab: d=224−250 μm

Szomolnokite, T=300K

lab: d=53-75 μm
lab: d=75-106 μm
lab: d=106-125 μm
lab: d=125-150 μm
lab: d=150-224 μm
lab: d=224-250 μm